Applied Physics Letters

Electron mobility in monolayer WS_2 encapsulated in hexagonal boron-nitride

Cite as: Appl. Phys. Lett. **118**, 102105 (2021); https://doi.org/10.1063/5.0039766
Submitted: 06 December 2020 . Accepted: 19 February 2021 . Published Online: 11 March 2021

Y. Wang, T. Sohier, K. Watanabe, T. Taniguchi, M. J. Verstraete, and E. Tutuc

© 2021 Author(s).

Applied Physics Letters ARTICLE scitation.org/journal/apl

Electron mobility in monolayer WS_2 encapsulated in hexagonal boron-nitride

Cite as: Appl. Phys. Lett. **118**, 102105 (2021); doi: 10.1063/5.0039766
Submitted: 6 December 2020 · Accepted: 19 February 2021 ·
Published Online: 11 March 2021

Y. Wang,[1] T. Sohier,[2] K. Watanabe,[3] T. Taniguchi,[4] M. J. Verstraete,[2] and E. Tutuc[1,a)]

AFFILIATIONS

[1]Microelectronics Research Center, Department of Electrical and Computer Engineering, The University of Texas at Austin, Austin, TX 78758, USA
[2]NanoMat/Q-Mat/CESAM, and European Theoretical Spectroscopy Facility, Université de Liege (B5), B-4000 Liege, Belgium
[3]Research Center for Functional Materials, National Institute of Materials Science, 1-1 Namiki, Tsukuba 305-0044, Japan
[4]International Center for Materials Nanoarchitectonics, National Institute for Materials Science, 1-1 Namiki, Tsukuba 305-0044, Japan

[a)]Author to whom correspondence should be addressed: etutuc@mail.utexas.edu

ABSTRACT

We report electron transport measurements in dual-gated monolayer WS_2 encapsulated in hexagonal boron-nitride. Using gated Ohmic contacts that operate from room temperature down to 1.5 K, we measure the intrinsic conductivity and carrier density as a function of temperature and gate bias. Intrinsic electron mobilities of 100 $cm^2/(V\,s)$ at room temperature and 2000 $cm^2/(V\,s)$ at 1.5 K are achieved. The mobility shows a strong temperature dependence at high temperatures, consistent with phonon scattering dominated carrier transport. At low temperature, the mobility saturates due to impurity and long-range Coulomb scattering. First-principles calculations of phonon scattering in monolayer WS_2 are in good agreement with the experimental results, showing we approach the intrinsic limit of transport in these two-dimensional layers.

Published under license by AIP Publishing. https://doi.org/10.1063/5.0039766

Transition metal dichalcogenides (TMDs) with the form MX_2 (M = Mo or W; X = S, Se, or Te) are layered materials, where each layer consists of two sheets of X atoms separated by one sheet of M atoms bonded covalently, while the different MX_2 layers are bonded by van der Waals forces.[1–3] This structure makes it possible to isolate individual two-dimensional (2D) layers, which possess significantly different properties compared with the bulk compound, due to quantum confinement effects.[4] Interesting electronic and photoelectronic properties are found in atomically thin TMDs, leading to many applications, such as high-ON/OFF-ratio field-effect transistors (FETs),[5–7] phototransistors,[8] and ultrasensitive photodetectors.[9] Valley polarization was also found in atomically thin TMDs as well as spin and valley Hall effects, stemming from coupled spin and valley degrees of freedom.[10–12] Tungsten disulfide (WS_2) is one member of the TMD family with an indirect bandgap of 1.3–1.4 eV in bulk form and a direct bandgap of 2.3–2.4 eV in monolayer form.[13,14] Theoretical calculations predict a lighter effective carrier mass for WS_2 among other TMDs, making it more attractive with potentially high carrier mobility and strong spin–orbit interaction.[15,16] Field-effect transistors based on few-layer WS_2 have been demonstrated down to monolayer thickness.[17,18] Photoluminescence (PL) studies have been performed on few-layer WS_2 as well, in which the evidence of strong spin-valley coupling was found.[19–21] However, little is known about the intrinsic electron transport, particularly in the monolayer limit.

In this work, we investigate the intrinsic electrical properties of dual-gated high-mobility FETs based on monolayer WS_2. The WS_2 FETs are encapsulated by atomically flat hexagonal boron-nitride (h-BN) membranes, which also act as top and back gate dielectric. The device active area is shaped into a Hall-bar, providing various measuring configuration options such as two-, four-point, and Hall effect measurements. We measure an intrinsic mobility of 2000 $cm^2/(V\,s)$ at the lowest temperatures and compare the two-, four-point field-effect, and intrinsic mobilities.

The monolayer WS_2 flakes used to fabricate WS_2 FETs are produced by regular or gold-assisted[22,23] micromechanical exfoliation, sourced from WS_2 crystals available commercially. The WS_2 flakes are exfoliated on a 285-nm-thick SiO_2 substrate, thermally grown on highly doped n-type silicon wafers. The flakes are identified by optical microscopy and then characterized by atomic force microscopy (AFM) and photoluminescence (PL). Figure 1(a) shows an optical

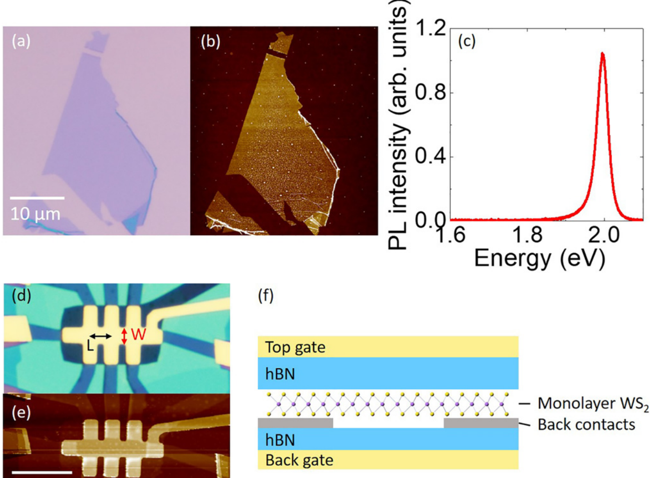

FIG. 1. (a) Optical micrography of a WS_2 monolayer on the SiO_2/Si substrate. (b) AFM topography of the same monolayer flake in (a). (c) Photoluminescence spectra acquired on the same flake shown in (a) and (b). (d) Optical micrography and (e) AFM topography of a dual-gated monolayer WS_2 device. (f) Schematic of the dual-gated monolayer WS_2 device structure.

micrograph of a micromechanically exfoliated monolayer WS_2 flake. The topography of the flake probed by AFM is shown in Fig. 1(b). A PL measurement is then performed on the same flake [Fig. 1(c)]. In contrast to the PL spectra of multi-layer WS_2, which have lower intensity and display multiple peaks associated with indirect gap transitions, the PL spectrum of the monolayer WS_2 exhibits a single peak at 2.0 eV associated with direct gap emission, consistent with previous observations.[4,19,21] This further confirms the thickness of the monolayer WS_2 flake.[19]

To electrically probe the monolayer WS_2 flakes, dual-gated WS_2 Hall bars with pre-patterned Pd or Pt bottom contacts are fabricated. The Pd or Pt contacts are thermally deposited on the bottom h-BN dielectric, placed on a local metal back gate. The monolayer WS_2 is transferred on the metal contacts by an h-BN flake picked up by a hemi-spherical shaped polypropylene carbonate/polydimethylsiloxane handle at 45 °C. The h-BN flakes used in this study are 10–25 nm thick. A metal top gate is then deposited to complete a dual-gated device. Figures 1(d) and 1(e) are the optical micrograph and AFM image of a monolayer WS_2 device (device A), respectively. The top gate is patterned in a Hall bar shape, defining the active area of the device. The schematic of the dual-gated device structure is shown in Fig. 1(f). Two dual-gated and h-BN encapsulated WS_2 monolayers are investigated in this study, labeled devices A and B.

Figure 2(a) shows the room temperature output characteristics, namely, drain current (I_D) vs drain voltage (V_D) measured at different top-gate voltages (V_{TG}), and at a back-gate bias $V_{BG} = 0$ V for device A. The linear $I_D - V_D$ response at low drain bias is indicative of Ohmic metal-to-WS_2 contacts. However, as we will show in this study, the metal-to-WS_2 contact resistance has a strong dependence on V_{TG}. Figure 2(b) shows the transfer characteristics, namely, I_D vs V_{TG} measured at drain biases $V_D = 0.05$ V and $V_D = 1$ V. Unlike a conventional FET, the I_D shows a strong, almost exponential dependence on

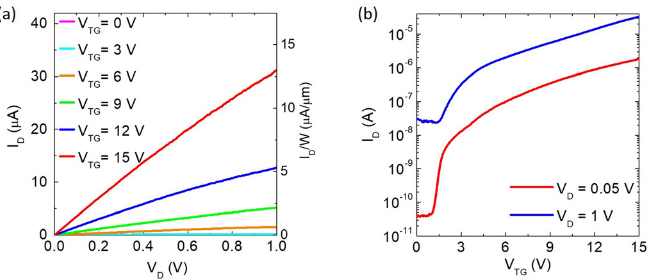

FIG. 2. (a) I_D vs V_D at various top gate biases. The linear dependence of $I_D - V_D$ is evidence of Ohmic contacts. (b) I_D vs V_{TG} at drain biases $V_D = 0.05$ V and 1 V. The ON/OFF ratio is around 10^5 at $V_D = 0.05$ V. The data were acquired at room temperature and in high vacuum.

V_{TG}, with a slope change at $V_{TG} \cong 2$ V, which represents the FET threshold voltage. The strong I_D vs V_{TG} dependence, both below and above threshold, is common to Schottky barrier FET characteristics and explained by a gate-dependent contact resistance. The top gate leakage current is lower than 1 nA in all measurements.

Magnetotransport measurements are carried out in perpendicular magnetic fields (B) up to 7 T, at a temperature $T = 100$ K. Figures 3(a)

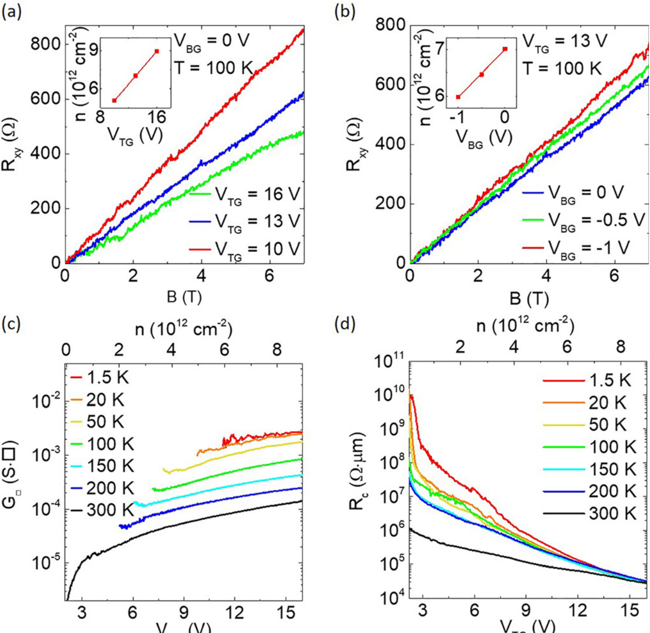

FIG. 3. (a) R_{xy} vs B measured for different V_{TG} values, at $V_{BG} = 0$ V and $T = 100$ K. (b) R_{xy} vs B measured for different V_{BG} values, at $V_{TG} = 13$ V and $T = 100$ K. R_{xy} is linearly dependent on B. Linear fits to R_{xy} vs B data yield the carrier densities. Insets: (a) n vs V_{TG} and (b) n vs V_{BG}; symbols represent the extracted values, and lines are the linear fits. (c) $G_{\square}$ vs V_{TG} and n (top axis) measured at various temperatures. The conductivity increases monotonically with decreasing temperature, suggesting a metallic phase. (d) R_c vs V_{TG} and n (top axis) at different temperatures. The contact resistance shows a strong dependence on V_{TG}, particularly at reduced temperatures. At high V_{TG}, the R_c values depend weakly on temperatures, consistent with tunneling through the Schottky barrier at the metal-to-WS_2 contact.

Published under license by AIP Publishing

and 3(b) show Hall resistance (R_{xy}) vs B at different V_{TG} [panel (a)] and V_{BG} [panel (b)] values. The slope of R_{xy} vs B data allows the extraction of the electron density (n) using $R_{xy}/B = 1/en$. Figures 3(a) and 3(b) insets show the extracted n vs V_{TG} and n vs V_{BG}, respectively. The linear fits to n vs V_{TG} and n vs V_{BG} yield the gate capacitances C_{TG} and C_{BG}, respectively. The carrier density can then be extracted at different gate biases via the relation $en = C_{TG}V_{TG} + C_{BG}V_{BG} + en_0$. The top gate capacitance of device A is $C_{TG} = 103\ nF/cm^2$, back gate capacitance $C_{BG} = 163\ nF/cm^2$, and $n_0 = -1.34 \times 10^{12}\,\mathrm{cm}^{-2}$. We assume that the same carrier density-gate bias relation holds for all temperatures for the following discussion. Using the outer contacts as the source and drain for current injection and the inner contacts as voltage probes (ΔV), we are able to measure the four-point channel conductance $G_{4pt} = I_D/\Delta V$ and intrinsic channel conductivity $G_\square = G_{4pt} \times L/W$, where $W = 2.4\,\mu$m is the width of the channel and $L = 3.5\,\mu$m is the distance between the medians of the neighboring contacts [Fig. 1(d)]. Figure 3(c) shows $G_\square$ vs V_{TG} and n at various temperatures ranging from 1.5 K to 300 K. We note that at reduced temperatures, the contact resistance increases at a fixed electron density, which in turn affects the accuracy of the four-point measurement. This is reflected in $G_\square$ vs n data of Fig. 3(c), where the accessible electron density range is gradually reduced with decreasing temperature. A linear dependence of $G_\square$ vs V_{TG} is observed at all temperatures. Furthermore, $G_\square$ increases monotonically with reducing T, indicating a metallic phase of 2D electrons in WS_2.

The four-point conductance G_{4pt} probes the intrinsic channel conductance compared to the two-point conductance $G_{2pt} = I_D/V_D$ because the former excludes contact resistances of the source and drain terminals. By subtracting the four-point resistance $1/G_{4pt}$ from the two-point resistance $1/G_{2pt}$, we can estimate the specific contact resistance $R_C = (1/G_{2pt} - 1/G_{4pt}) \times W_C/2$, where W_C represents the contact width of the source/drain terminal. The R_C vs V_{TG} and n measured at various T values are shown in Fig. 3(d). At low electron densities, the contact resistance has a strong temperature dependence and increases with reducing temperature. This observation can be explained by a diminished thermally activated injection over the metal-to-WS_2 Schottky barrier. However, at high electron densities, the contact resistance becomes less sensitive to temperature and remains relatively low down to 1.5 K. The insensitivity to temperature suggests the electron injection is controlled by tunneling through the Schottky barrier at the metal-to-WS_2 contact, which in turn is achieved by inducing a large electron density in the channel around the metal-to-WS_2 interface, resulting in a tunnel barrier with reduced thickness.[24,25]

The intrinsic carrier mobility $\mu = G_\square/(ne)$ can be calculated using the measured $G_\square$ and n values. Absent carrier density measurements, a separate and often used metric is the two- or four-point field-effect mobility $\mu_{FE} = (L/W) \times (dG/dV_G) \times C_G^{-1}$, where G is the two- or four-point conductance and V_G and C_G are the top/back gate bias and capacitance. To assess the accuracy of this metric, we compare the two- and four-point μ_{FE} with the intrinsic μ value. Figure 4(a) shows μ vs T at different n values, along with μ_{FE} vs T extracted from G_{4pt} vs V_{TG} data. At room temperature, the intrinsic mobility at the highest electron density $9 \times 10^{12}\,\mathrm{cm}^{-2}$ is $100\,\mathrm{cm}^2/(\mathrm{V\,s})$ and increases rapidly with decreasing temperature, reaching $2000\,\mathrm{cm}^2/(\mathrm{V\,s})$ at 1.5 K. At high temperature ($T > 50$ K), the temperature dependence of the mobility follows approximately a power law $\mu \propto T^{-\gamma}$, and a functional

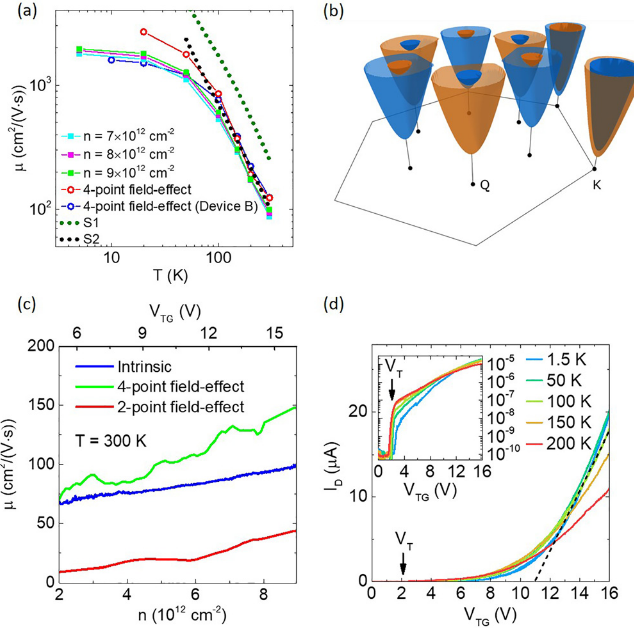

FIG. 4. (a) Temperature dependence of the measured intrinsic and field-effect mobility (symbols). Unless noted, the data are acquired on device A. For $T > 50$ K, a strong temperature dependence suggests phonon scattering dominated transport. The mobility saturates at $T < 50$ K, limited by long-range Coulomb scattering. First-principles calculations (dashed lines) are performed at an electron density $n = 8 \times 10^{12}\,\mathrm{cm}^{-2}$, using two different structures, S1 and S2, leading to K–Q valley splittings of 90 meV and 54 meV, respectively. (b) Schematic of the multivalley, spin-textured band structure of WS_2 showing only the inequivalent K and Q valleys in one Brillouin zone. Orange and blue colors represent opposite spin-textures. (c) μ vs n at room temperature. The comparison includes the intrinsic mobility, as well as the two- and four-point field-effect mobilities. The bottom and top axes are Hall density and top gate bias, respectively. The four-point field-effect mobility overestimates the intrinsic mobility, while two-point field-effect mobility underestimates the intrinsic mobility by approximately 50%. (d) Temperature dependence of I_D vs V_{TG}, on a linear scale and log-linear scale (inset), measured at $V_D = 0.5$ V. The arrows mark the V_T extracted from the Hall density measurements. A linear extrapolation of the I_D vs V_{TG} data (dashed line) intercepts the V_{TG} axis at a value significantly larger than V_T.

fit of the data yields $\gamma = 1.46$. Intravalley scattering from zone center acoustic phonons in a deformation potential model leads to $\gamma = 1$.[26] Thus, $\gamma > 1$ suggests a more complex combination of both intra- and intervalley contributions from acoustic and optical phonons, which we confirm through first-principles calculations. At low temperature, the mobility saturates at $\sim 2000\,\mathrm{cm}^2/(\mathrm{V\,s})$, which can be explained by long-range Coulomb scattering.[27]

In Fig. 4(a), the experimental mobility values are compared with first-principles calculations of the intrinsic, phonon-limited mobility of WS_2, which show good agreement with the measurements. The electron–phonon interactions are computed within density-functional perturbation theory[28,29] and optimized norm-conserving Vanderbilt pseudopotentials[30] from the PseudoDojo library.[31] The full momentum- and energy-dependent Boltzmann transport equation is solved iteratively as detailed in Ref. 32. An electrostatic doping of $8 \times 10^{12}\,\mathrm{cm}^{-2}$ is explicitly included[33] to account for free-carrier screening and the enhancement of electron–phonon scattering

Published under license by AIP Publishing

induced by multivalley occupation in TMDs.[34] Spin–orbit interaction is included in all simulations, augmenting Ref. 32. As depicted in Fig. 4(b), the conduction band is composed of K and Q valleys, each split by spin–orbit interactions.

Transport simulations are highly sensitive to the details of this complex band structure and, in particular, to the relative positions of the valleys and the Fermi level, which are in turn sensitive to the computational details. In an effort to capture this, Fig. 4(a) reports mobility for two slightly different structures: S1 and S2. The lattice parameters are identical ($a_1 = a_2 = 3.187$ Å) while the layer thickness in S2 is just 0.4% larger ($t_1 = 3.14$ Å and $t_2 = 3.15$ Å), which is within density-functional theory structural precision. Both structures are realistic, and a similar variation in thickness may occur in real devices due to encapsulation or substrate interaction. The K–Q valley splittings are 90 meV for S1 and 54 meV for S2, respectively. Small variations are also present in the Fermi velocity ($\sim$10% smaller for S2) and the spin–orbit splitting at the K point (30 meV for S1 vs 33 meV for S2). Many-body, polaronic, and other encapsulation effects could have a comparable impact. The mobility values calculated using setup S1 are higher compared to setup S2 mainly because of the higher Q valley energy, which suppresses K–Q intervalley scattering[32] and allows free carriers to screen the coupling to homopolar optical phonons.[34] The agreement between experiment and simulations is good in magnitude and in the temperature dependence above 50 K. We conclude that the experimental results are very close to the intrinsic, phonon-limited regime and that the electron–phonon physics is fully captured by the simulations.

In Fig. 4(c), we compare the intrinsic, two-point, and four-point field-effect mobilities at room temperature. The four-point field-effect values are consistently larger compared to the intrinsic mobility, similar to observations reported in MoS_2 FETs.[5] To explain this observation, let us assume the dielectric-TMD interface has a density (D_{it}) of traps per unit area$\times$energy at the Fermi energy. A change in gate bias (dV_G) will induce a change in both the density of the trapped charges dn_{it} and the mobile electron density dn, $C_G dV_G = e(dn_{it} + dn)$. In thermodynamic equilibrium, $dn_{it}/dn = D_{it}/DOS$, where DOS is the density of states of the 2D system at the Fermi energy. The four-point field effect mobility then writes

$$\mu_{FE} = \frac{1}{C_G} \cdot \frac{dG_\square}{dn} \cdot \frac{dn}{dV_G} = \frac{\mu + n(d\mu/dn)}{1 + D_{it}/DOS}. \tag{1}$$

For a TMD layer with twofold valley degeneracy, $DOS = 2m^*/(\pi\hbar^2)$, where m^* is the effective mass and $\hbar$ is the reduced Planck constant. Using $m^* = 0.5m_e$, a typical value for TMDs, the corresponding $DOS = 4 \times 10^{14}\,\text{cm}^{-2}\,\text{eV}^{-1}$. The intrinsic defect density in exfoliated TMDs determined from scanning probe microscopy is $\sim 10^{12}\,\text{cm}^{-2}$,[35,36] and even for a gate-stack of moderate quality, the corresponding D_{it} should be at least one order of magnitude lower compared to DOS. As such, the ratio D_{it}/DOS can safely be neglected in Eq. (1) when the 2D layer is populated with carriers, and the Fermi energy is above the band edge. This approximation is also supported by the very good agreement between the geometric gate capacitances and their values determined by Hall measurements in our experiment. Equation (1) then writes $\mu_{FE} - \mu = n(d\mu/dn)$. If the μ value increases with n, which is expected if screening plays a role in the scattering mechanism, the four-point field-effect mobility will overestimate the intrinsic mobility. We note that scattering mechanisms such as surface roughness or carrier confinement which normally lead to a reduction in mobility at high carrier densities in inversion layers realized in bulk semiconductors either do not apply or do not have the same density dependence in 2D materials. Indeed, the surface roughness is not expected to reduce the mobility at high densities in 2D materials because the electron wave-function does not change appreciably with gate bias. Moreover, the confinement in the 2D plane does not lead to multiple subbands as one might encounter in the triangular well of a metal-oxide-semiconductor FET.

It is noteworthy that the two-point field-effect mobility significantly underestimates the mobility by $\sim$50%, which can be attributed to the voltage drop on the source/drain and the gate-dependent contact resistances. To better illustrate the differences between the WS_2 FET characteristics and conventional FETs with highly doped source and drain, in Fig. 4(d), we show the temperature dependence of transfer characteristics, I_D vs V_{TG} measured at $V_D = 0.5$ V. The main panel in Fig. 4(d) shows that a linear extrapolation of the I_D vs V_{TG} intercepts the x-axis at $V_{TG} \cong 11$ V, a value significantly larger than the threshold voltage $V_T = 2.1$ V at which the Hall density $n = 0$. Therefore, applying a conventional FET analysis will largely overestimate the threshold voltage and underestimate the carrier density at a given V_{TG} value. In the inset of Fig. 4(d), we show the same dataset on a log-linear scale, along with the V_T determined from Hall measurements. Similar to Fig. 2(b) data, I_D has an exponential dependence on V_{TG}, with a marked change in slope at $V_{TG} \approx V_T$. This dataset suggests that a better V_T estimation can be obtained from the V_{TG} value at which the exponential I_D vs V_{TG} dependence changes slope. Finally, we note that the V_T is weakly dependent on temperature. The variation of the threshold voltage over the range of temperature in our study is ~ 0.5 V, corresponding to a carrier density variation of $3 \times 10^{11}\,\text{cm}^{-2}$.

To conclude, we have demonstrated high-quality dual-gated monolayer WS_2 field-effect transistors encapsulated in h-BN, with Ohmic contacts at temperatures down to 1.5 K. Magnetotransport measurements were performed, and carrier densities and intrinsic mobilities were extracted from Hall effect measurements. A high electron mobility of $2000\,\text{cm}^2/(\text{V s})$ was measured at 1.5 K. In addition, we compared three methods to evaluate electron mobility and conclude that two- and four-point field-effect mobilities underestimate and overestimate carrier mobilities in 2D TMD systems, respectively. Good agreement with first-principles calculations of the phonon-limited mobility of WS_2 confirms the quality of the devices and indicates transport properties close to the intrinsic limit.

The work at the University of Texas at Austin was supported by Army Research Office under Grant No. W911NF-17-1-0312, the National Science Foundation under Grants No. DMR-1720595 and EECS-1610008, and the Welch Foundation under Grant No. F-2018-20190330. K.W. and T.T. acknowledge support from the Elemental Strategy Initiative conducted by the MEXT, Japan, Grant No. JPMXP0112101001, JSPS KAKENHI Grant No. JP20H00354, and the CREST (No. JPMJCR15F3), JST.

The results of this research have been partially achieved using the DECI resource ARCHER UK National Supercomputing Service with support from the PRACE aisbl. Simulation time was also awarded by PRACE (Project Id: 2020225411) on MareNostrum at Barcelona Supercomputing Center-Centro Nacional de Supercomputación

Published under license by AIP Publishing

(The Spanish National Supercomputing Center) and by the Consortium des Equipements de Calcul Intensif (CECI), funded by the Fonds de la Recherche Scientifique de Belgique (FNRS) under Grant No. 2.5020.11 and by the Walloon Region. T.S. acknowledges support from NCCR MARVEL funded by the Swiss National Science Foundation and from the University of Liege under the Special Funds for Research, IPD-STEMA Programme. M.J.V. gratefully acknowledges funding from the Belgian FNRS under PDR Grant No. T.0103.19-ALPS and from the MELODICA project, funded by the EU FLAG-ERA JTC2017 call.

DATA AVAILABILITY

The data that support the findings of this study are available from the corresponding author upon reasonable request.

REFERENCES

[1] J. A. Wilson and A. D. Yoffe, Adv. Phys. **18**, 193 (1969).
[2] Q. H. Wang, K. Kalantar-Zadeh, A. Kis, J. N. Coleman, and M. S. Strano, Nat. Nanotechnol. 7, 699 (2012).
[3] M. Chhowalla, H. S. Shin, G. Eda, L.-J. Li, K. P. Loh, and H. Zhang, Nat. Chem. **5**, 263 (2013).
[4] W. Zhao, Z. Ghorannevis, L. Chu, M. Toh, C. Kloc, P.-H. Tan, and G. Eda, ACS Nano **7**, 791 (2013).
[5] B. W. H. Baugher, H. O. H. Churchill, Y. Yang, and P. Jarillo-Herrero, Nano Lett. **13**, 4212 (2013).
[6] H. C. P. Movva, A. Rai, S. Kang, K. Kim, B. Fallahazad, T. Taniguchi, K. Watanabe, E. Tutuc, and S. K. Banerjee, ACS Nano **9**, 10402 (2015).
[7] C. Gong, Y. Zhang, W. Chen, J. Chu, T. Lei, J. Pu, L. Dai, C. Wu, Y. Cheng, T. Zhai, L. Li, and J. Xiong, Adv. Sci. **4**, 1700231 (2017).
[8] Z. Yin, H. Li, H. Li, L. Jiang, Y. Shi, Y. Sun, G. Lu, Q. Zhang, X. Chen, and H. Zhang, ACS Nano **6**, 74 (2012).
[9] O. Lopez-Sanchez, D. Lembke, M. Kayci, A. Radenovic, and A. Kis, Nat. Nanotechnol. **8**, 497 (2013).
[10] T. Cao, G. Wang, W. Han, H. Ye, C. Zhu, J. Shi, Q. Niu, P. Tan, E. Wang, B. Liu, and J. Feng, Nat. Commun. **3**, 887 (2012).
[11] K. F. Mak, K. L. McGill, J. Park, and P. L. McEuen, Science **344**, 1489 (2014).
[12] C. K. Safeer, J. Ingla-Aynés, F. Herling, J. H. Garcia, M. Vila, N. Ontoso, M. R. Calvo, S. Roche, L. E. Hueso, and F. Casanova, Nano Lett. **19**, 1074 (2019).
[13] A. Chernikov, T. C. Berkelbach, H. M. Hill, A. Rigosi, Y. Li, O. B. Aslan, D. R. Reichman, M. S. Hybertsen, and T. F. Heinz, Phys. Rev. Lett. **113**, 076802 (2014).
[14] W.-T. Hsu, J. Quan, C.-Y. Wang, L.-S. Lu, M. Campbell, W.-H. Chang, L.-J. Li, X. Li, and C.-K. Shih, 2D Mater. **6**, 025028 (2019).
[15] A. Kormányos, V. Zólyomi, N. D. Drummond, and G. Burkard, Phys. Rev. X **4**, 011034 (2014).
[16] Z. Jin, X. Li, J. T. Mullen, and K. W. Kim, Phys. Rev. B **90**, 045422 (2014).
[17] M. W. Iqbal, M. Z. Iqbal, M. F. Khan, M. A. Shehzad, Y. Seo, J. H. Park, C. Hwang, and J. Eom, Sci. Rep. **5**, 10699 (2015).
[18] Y. Cui, R. Xin, Z. Yu, Y. Pan, Z.-Y. Ong, X. Wei, J. Wang, H. Nan, Z. Ni, Y. Wu, T. Chen, Y. Shi, B. Wang, G. Zhang, Y.-W. Zhang, and X. Wang, Adv. Mater. **27**, 5230 (2015).
[19] H. Zeng, G.-B. Liu, J. Dai, Y. Yan, B. Zhu, R. He, L. Xie, S. Xu, X. Chen, W. Yao, and X. Cui, Sci. Rep. **3**, 1608 (2013).
[20] H. R. Gutiérrez, N. Perea-López, A. L. Elías, A. Berkdemir, B. Wang, R. Lv, F. López-Urías, V. H. Crespi, H. Terrones, and M. Terrones, Nano Lett. **13**, 3447 (2013).
[21] S. Jo, N. Ubrig, H. Berger, A. B. Kuzmenko, and A. F. Morpurgo, Nano Lett. **14**, 2019 (2014).
[22] S. B. Desai, S. R. Madhvapathy, M. Amani, D. Kiriya, M. Hettick, M. Tosun, Y. Zhou, M. Dubey, J. W. Ager, D. Chrzan, and A. Javey, Adv. Mater. **28**, 4053 (2016).
[23] M. Velický, G. E. Donnelly, W. R. Hendren, S. McFarland, D. Scullion, W. J. I. DeBenedetti, G. C. Correa, Y. Han, A. J. Wain, M. A. Hines, D. A. Muller, K. S. Novoselov, H. D. Abruña, R. M. Bowman, E. J. G. Santos, and F. Huang, ACS Nano **12**, 10463 (2018).
[24] J. Appenzeller, M. Radosavljević, J. Knoch, and Ph. Avouris, Phys. Rev. Lett. **92**, 048301 (2004).
[25] S. Das, H.-Y. Chen, A. V. Penumatcha, and J. Appenzeller, Nano Lett. **13**, 100 (2013).
[26] K. Kaasbjerg, K. S. Thygesen, and K. W. Jacobsen, Phys. Rev. B **85**, 115317 (2012).
[27] N. Ma and D. Jena, Phys. Rev. X **4**, 011043 (2014).
[28] P. Giannozzi, S. Baroni, N. Bonini, M. Calandra, R. Car, C. Cavazzoni, D. Ceresoli, G. L. Chiarotti, M. Cococcioni, I. Dabo, A. Dal Corso, S. de Gironcoli, S. Fabris, G. Fratesi, R. Gebauer, U. Gerstmann, C. Gougoussis, A. Kokalj, M. Lazzeri, L. Martin-Samos, N. Marzari, F. Mauri, R. Mazzarello, S. Paolini, A. Pasquarello, L. Paulatto, C. Sbraccia, S. Scandolo, G. Sclauzero, A. P. Seitsonen, A. Smogunov, P. Umari, and R. M. Wentzcovitch, J. Phys. **21**, 395502 (2009).
[29] P. Giannozzi, O. Andreussi, T. Brumme, O. Bunau, M. Buongiorno Nardelli, M. Calandra, R. Car, C. Cavazzoni, D. Ceresoli, M. Cococcioni, N. Colonna, I. Carnimeo, A. Dal Corso, S. de Gironcoli, P. Delugas, R. A. DiStasio, A. Ferretti, A. Floris, G. Fratesi, G. Fugallo, R. Gebauer, U. Gerstmann, F. Giustino, T. Gorni, J. Jia, M. Kawamura, H.-Y. Ko, A. Kokalj, E. Küçükbenli, M. Lazzeri, M. Marsili, N. Marzari, F. Mauri, N. L. Nguyen, H.-V. Nguyen, A. Otero-de-la-Roza, L. Paulatto, S. Poncé, D. Rocca, R. Sabatini, B. Santra, M. Schlipf, A. P. Seitsonen, A. Smogunov, I. Timrov, T. Thonhauser, P. Umari, N. Vast, X. Wu, and S. Baroni, J. Phys. **29**, 465901 (2017).
[30] D. R. Hamann, Phys. Rev. B **88**, 085117 (2013).
[31] M. J. van Setten, M. Giantomassi, E. Bousquet, M. J. Verstraete, D. R. Hamann, X. Gonze, and G.-M. Rignanese, Comput. Phys. Commun. **226**, 39 (2018).
[32] T. Sohier, D. Campi, N. Marzari, and M. Gibertini, Phys. Rev. Mater. **2**, 114010 (2018).
[33] T. Sohier, M. Calandra, and F. Mauri, Phys. Rev. B **96**, 075448 (2017).
[34] T. Sohier, E. Ponomarev, M. Gibertini, H. Berger, N. Marzari, N. Ubrig, and A. F. Morpurgo, Phys. Rev. X **9**, 031019 (2019).
[35] R. Addou, L. Colombo, and R. M. Wallace, ACS Appl. Mater. Interfaces **7**, 11921 (2015).
[36] C.-P. Lu, G. Li, J. Mao, L.-M. Wang, and E. Y. Andrei, Nano Lett. **14**, 4628 (2014).

Published under license by AIP Publishing